Wearable Microneedle-based Array Patches for the Continuous Electrochemical Monitoring and Drug Delivery: Towards a Closed-loop System for Methotrexate Treatment

Marc Parrilla,[a,b,*] Usanee Detamornrat,[c] Juan Domínguez-Robles,[c] Sensu Tunca,[a,b] Ryan F. Donnelly,[c,*] Karolien De Wael[a,b,*]

[a] A-Sense Lab, Department of Bioscience Engineering, University of Antwerp, Groenenborgerlaan 171, 2020 Antwerp, Belgium.

[b] NANOlab Center of Excellence, University of Antwerp, Groenenborgerlaan 171, 2020, Antwerp, Belgium

[c] School of Pharmacy, Medical Biology Centre, Queen's University Belfast, 97 Lisburn Road, Belfast BT9 7BL, United Kingdom.

*Corresponding author

ABSTRACT

Wearable devices based on microneedle (MN) technology have recently emerged as tools for *in situ* transdermal sensing or delivery in interstitial fluid (ISF). Particularly, MN-based electrochemical sensors allow the continuous monitoring of analytes in a minimally invasive manner through ISF. Exogenous small molecules found in ISF such as therapeutic drugs are ideal candidates for MN sensors due to their correlation with blood levels and their relevance for the optimal management of personalized therapies. Herein, a hollow MN array patch is modified with conductive pastes and functionalized with crosslinked chitosan to develop a MN-based voltammetric sensor for continuous monitoring of methotrexate (MTX). Interestingly, the chitosan coating avoids biofouling while enabling the adsorption of MTX at the electrode's surface for sensitive analysis. The MN sensor exhibits excellent analytical performance *in vitro* with protein-enriched artificial ISF and *ex vivo* under a Franz diffusion cell configuration. The MN sensor shows a linear range from 25 to 400 µM, which fits within the therapeutic range of high-dose MTX treatment for cancer patients, and an excellent continuous operation for more than two days. Moreover, an iontophoretic hollow MN array patch is developed with the integration of both anode and cathode in the single MN array patch. The *ex vivo* characterization demonstrates the transdermal on-demand drug delivery of MTX. Overall, the combination of both MN patches represents impactful progress in closed-loop systems for therapeutic drug management in disorders such as cancer, rheumatoid arthritis, or psoriasis.

KEYWORDS

Hollow microneedle array, wearable electrochemical sensor, microneedle-based sensor, microneedle-based drug delivery, voltammetric sensor, methotrexate monitoring, therapeutic drug monitoring, chemotherapy.

Wearable electrochemical devices have revolutionized how chemical data is collected and analyzed on the spot.[1,2] The most successful example is the continuous glucose monitoring system used by many diabetic patients, highlighting its improvement in disease management. Such a system is based on an integrated electrochemical sensor embedded in a tiny needle that pierces the outer layer of the skin to reach interstitial fluid (ISF) for glucose sensing.[3] However, the insertion and the length of the needle make the process cumbersome and painful, respectively. To overcome these issues, microneedle (MN) array patches have been modified with conductive materials to be used as electrochemical sensors,[4–6] being the majority of the state-of-the-art for glucose monitoring.[7]

Wearable MN-based electrochemical sensors have been produced under different configurations: (i) a conductive solid MN array to attain an electrode;[8,9] (ii) a hollow MN array (HMA) filled with conductive pastes to attain an electrochemical cell;[10,11] (iii) a HMA used for the extraction of ISF toward an electrochemical sensor at the back side of the HMA;[12] or (iv) a polymeric MN array with the capability to uptake ISF that contains an inserted miniaturized electrode/sensor.[13]

MN-based transdermal diagnostics is, therefore, an appealing technology to monitor analytes in ISF due to its minimal invasiveness and huge availability of the skin ISF in comparison to blood. However, the partitioning of analytes in dermal ISF needs to be considered when designing MN-based sensors.[14] The selection of the analyte needs to be previously evaluated, considering its size, charge, percentage of analyte bound to proteins, and presence in ISF.[14] Ideally, small molecules (e.g. glucose, ions, urea, drugs or cytokines) up to 3 kDa can easily diffuse through blood capillaries to ISF, becoming thus available for the MN sensors at similar levels to the blood. Hence, there is a rising interest in drug monitoring through ISF due to the opportunities that electrochemical sensors offer in drug detection, particularly fitting the therapeutic range, sensitivity and limit of detection (LOD).[15,16] Unfortunately, larger macromolecules are found at lower levels in ISF than in blood which makes it challenging for MN sensors with the need for extremely low LOD.[14]

MNs arrays have been used for drug monitoring.[15,17] Mainly, three strategies are approached for drug monitoring: (i) the use of direct electrochemical oxidation at the surface of the HMA electrode for apomorphine[11] or levodopa[18]; (ii) the functionalization of solid MNs with aptamers for different antibiotics;[9,19] and (iii) the use of swellable MNs mounted on interdigitated electrodes for levodopa detection.[20]

The integration of electrochemical sensors with MN patches for on-demand drug delivery[21] is bringing an advent in closed-loop systems for optimal drug delivery.[22,23] These closed-loop systems are mainly built on electrochemical devices,[15] offering an opportunity to develop wearable self-powered devices.[2] For example, a fully integrated closed-loop system based on mesoporous MNs-iontophoresis was reported for self-sufficient diabetes treatment.[24] Similarly, MNs were functionalized as biosensors and combined with an electroosmotic pump to deliver insulin.[25] Recently, an ultrasonic insulin pump was integrated with a MN sensor for on-demand delivery.[26] These systems could deliver an appropriate insulin dose depending on the glucose level of the patient, empowering future personalized medicine. Principally, closed-loop systems are designed for diabetes management. However, many other disorders could benefit from this technology.[27]

Methotrexate (MTX) is a widely used drug for the treatment of cancer, rheumatoid arthritis, and psoriasis, among others.[28,29] For example, MTX has been transdermally delivered using dissolving MNs for the treatment of psoriasis.[30] In cancer treatment, the levels of MTX of a patient under high-dose MTX expand from high (mM range) to low concentration (μM range). The levels determine the toxicity to the body e.g. if the MTX blood concentration is >10 μM at 24 h post-administration, the patient needs to be rescued with leucovorin.[29,31] Therefore, the ability to rapidly detect MTX (toxic) levels in the human body is essential for the safety of the patient while providing optimal treatment. Indeed, the continuous monitoring of MTX has been recently achieved by aptamer-based sensors.[32] Importantly, MTX is electroactive at physiological pH on carbon-based electrodes.[33,34] This opens the possibility to use MN-based electrochemical sensors for its detection in ISF. However, the challenges remain in the engineering of the MN sensor, the stability for continuous operation, and the ability to reduce biofouling for undiluted analysis in biofluids.

Herein, the first MN-based electrochemical sensor for transdermal MTX monitoring is presented. First, hollow MNs are modified with conductive pastes, and subsequently, the working electrode is functionalized with chitosan (CHI) crosslinked with glutaraldehyde (GA) to provide the sensor with anti-biofouling and preconcentration capabilities (**Figure 1A**). This CHI-GA coating enables the operation within the therapeutic range of high-dose MTX treatment. The coating facilitates the adsorption of MTX at the electrode's surface while avoiding protein diffusion to the electrode. The analytical characterization of the functionalized microneedle (f-MN) sensor has been executed *in vitro* under protein-enriched artificial interstitial fluid (AISF) and *ex vivo* by piercing the f-MN sensor in porcine skin employing a Franz diffusion cell setup. Finally, a MN-based drug delivery system for MTX is designed utilizing an iontophoretic hollow microneedle array system (IHMAS) (**Figure 1B**). The device has been successfully characterized under the *ex vivo* setup. These MN patches generate the preliminary steps toward a closed-loop system for MTX treatment. Overall, the current work

3

presents a leap forward in the field of MN devices for decentralized and digitized healthcare while providing technology for patient-centered remote monitoring.
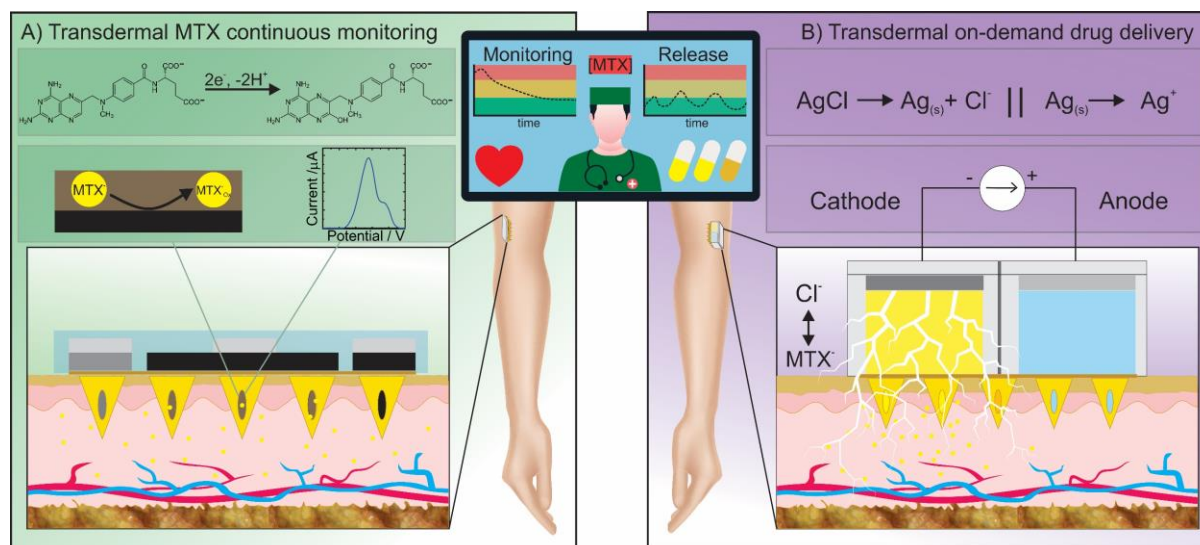
Figure 1. *Wearable microneedle array patch for the continuous electrochemical monitoring and drug delivery of MTX: (A) Schematics of the functionalized microneedle sensor for transdermal monitoring of MTX. (B) Illustration of the iontophoretic microneedle array system for transdermal on-demand drug delivery of MTX.*

EXPERIMENTAL SECTION

Fabrication of the MN patch for drug monitoring. The HMA consists of 5 x 5 pyramidal-shaped MNs with 1 mm height, 0.75 mm width, 2 mm tip-to-tip interspacing, and 100 μm hole diameter (**Figure S1A** and dimensions **Table S1**). Detailed information on the evaluation of the piercing capability of the HMA and images of the piercing tests are described in the supporting information (SI) and **Figure S2** and **Figure S3**, respectively.

The MN sensing patch was fabricated by filling the holes with the appropriate conductive paste to form a three-electrode electrochemical cell (**Figure S4A and S4B**). Thus, the MN sensor incorporates a working electrode (WE) and counter electrode (CE) based on graphite paste, and a reference electrode (RE) based on silver/silver chloride (Ag/AgCl) paste. Further information on the materials is described in the SI. Once the hole of each MN is filled by using a spatula, the excess of the corresponding paste was carefully removed from the hole using a scalpel following the angle of the MN. This is a critical step to avoid any paste above the MN as the polymeric material of the MN needs to protect the electrode (**Figure S5**). Thereafter, conductive pastes were cured at 80 °C for 30 min in an oven. Electrical contacts were established using a screen-printed planar connector on a PET substrate at the backside of each of the conductive pastes to realize the MN sensor (**Figure S4C** and **S4D**). Glue is used to isolate the edges of the MN sensor and avoid the solution to leak into the connections. Finally, the crosslinked CHI solution (prepared from a 1.5% CHI in 2% acetic acid diluted to a 0.15% CHI aqueous solution and mixed

with GA solution to obtain a 5% GA) was deposited on the MNs WE (70 μL) and let dry in the oven at 40 °C for 30 min. **Figures S4E** and **S4F** depict the CHI layer on top of the MN WE. Details on the fabrication of the HMN patch for drug delivery, preparation of the drug-loaded hydrogel, *in vitro* drug delivery study, *ex vivo* drug permeation study, and statistical analysis are described in SI and in **Figure S6**. Details on the characterization of the sensor and the *in vitro* and *ex vivo* (**Figure S7**) analytical characterization of the MN sensor are described in the SI.

RESULTS AND DISCUSSION

Development of the MN patch for drug monitoring.

The HMA was modified with conductive pastes (details in the experimental section) to develop a MN-based electrochemical sensor (**Figure S4**). The WE consists of 12 MNs, the RE consists of five MNs and the CE consists of eight MNs (**Figure S1**). The distribution of the electrodes followed the same configuration used in screen-printed electrodes.[35] The WE was subsequently functionalized with the crosslinked CHI/GA solution by dropping the solution on top of the WE and letting it dry. This functionalization provides anti-biofouling and adsorption capabilities to the WE, allowing the continuous monitoring of MTX in biofluids. First, a regular SPE was employed as a model electrode to study the morphology under scanning electron microscopy (SEM) of the deposited CHI layer with and without crosslinker. **Figures S8A** and **S8B** depict the surface of a bare graphite electrode in the SPE, showing its rough structure with graphite flakes as previously reported.[36] **Figures S8C** and **S8D** show the surface of the graphite electrode with the deposited CHI layer (no crosslinking). The SEM images display similar shapes as per the bare graphite electrode, meaning that the CHI coating remained highly porous on the electrode. In contrast, crosslinked CHI coating exhibited a very smooth layer on top of the graphite, proving the crosslinking activity on the coating (**Figures S8E** and **S8F**).

The morphology and distribution of the crosslinked CHI/GA coating on the MN-based electrodes were also characterized by SEM. **Figures S8G**, **S8H** and **S8I** depict the modified MN RE at different magnifications. **Figure S8I** shows the silver particles embedded in the polymeric paste. **Figures S8J**, **S8K** and **S8L** display the crosslinked CHI/GA deposited on the MN WE. The images show the formation of a smooth coating on the electrodes. To evaluate the thickness of the coating, a MN sensor with a scratched crosslinked CHI/GA layer was analyzed (**Figures S5G-S5I**). **Figures S8M** and **S8N** depict a piece of the crosslinked coating at the base of the MN sensor exhibiting a thickness of 9.0 ± 0.6 μm (N = 3). **Figures S8O** and **S8P** display the thickness of 4.8 ± 0.1 μm (N = 3) at the MN body. It is suggested that the thickness at the body is less than at the base as a higher amount of solution is accumulated at the base of the MN during the evaporation of the solvent. Finally, **Figures S8Q**, **S8R** and **S8S** show the SEM images of the MN CE, exhibiting a morphology similar to the graphite bare electrode.

The deposition of the CHI and crosslinked CHI/GA coatings were characterized with ATR-FTIR. The coatings were first deposited on planar SPEs to allow direct analysis with the ATR module. **Figure S9** shows the FTIR spectra of CHI and crosslinked CHI/GA coating confirming the reaction of the amino groups with GA. Both the NH_2 stretching bands at 3349 and 3283 cm^{-1}, which are observed in the CHI spectrum, could not be observed in the spectrum of the crosslinked coating.[37] Moreover, a characteristic peak at 1150 cm^{-1} associated with C-O-C bridges was shifted to a prominent 1110 cm^{-1} peak.[38]

Synergic effect of the crosslinked chitosan coating for methotrexate sensing.

The modification of electrodes with nanomaterials has proved to be an effective solution to improve the sensitivity and reach a low limit of detection.[39] However, the use of these modifications on biofluids for continuous monitoring is hindered by protein adsorption. Therefore, the use of crosslinked CHI/GA is an effective manner to provide continuous monitoring of MTX in biofluids. To evaluate the synergic effect of the crosslinked chitosan coating for MTX sensing, SPEs were modified with a CHI and crosslinked CHI/GA. A preliminary optimization of the crosslinking ratio of the CHI membrane was performed. An optimal ratio of 0.1 (i.e. composition of 0.15% CHI and 1.5 % GA) was obtained showing an increment of 3.9-fold in comparison to a bare SPE for 50 µM MTX in PBS (**Table S2**). **Figures S10A-S10C** depict the electrochemical oxidation of MTX on bare, CHI- and CHI/GA-coated SPEs in PBS after 10 min adsorption time. The anodic signal was dramatically enhanced at the crosslinked CHI/GA coated electrode for the oxidation of 100 and 300 µM MTX in PBS pH 7.4, exhibiting an increment in peak current (I_p) of 4.2 ± 0.2 fold and 3.0 ± 0.2 fold in comparison to the bare and CHI-coated SPEs, respectively. Importantly, the CHI/GA-coated SPE displayed a 7.9 ± 1.6 fold and 2.85 ± 1.0 fold increment in the I_p when the electrodes were interrogated in PBS with BSA (**Figures S10D-S10F**). This suggests that the CHI layer provides the anti-biofouling capability to the sensor, but CHI/GA is necessary for highly sensitive detection due to the MTX adsorption in the coating. Moreover, the oxidation potential of the CHI/GA-coated SPEs in BSA-enriched solution decreased from 0.92 V at bare SPE to 0.85 V at CHI-coated and 0.78 V at CHI/GA-coated SPEs. The adsorption hypothesis was verified by executing a scan rate study to evaluate the mass transport behavior at the CHI/GA electrode. **Figure S11A** shows the cyclic voltammograms of 500 µM MTX at different scan rates (i.e. 0.025 – 0.75 V s^{-1}). Subsequently, the anodic contribution (I_p) was plotted against the scan rate (**Figure S11B**). A linear relationship was obtained corresponding to an adsorption-controlled process. Besides, the I_p was represented against the square root of the scan rate showing a non-linear behavior (**Figure S11C**). Finally, the logarithm of the I_p and scan rate was displayed exhibiting a slope of 0.76 which is higher than the theoretical value of the diffusion-controlled process (i.e. 0.5) (**Figure S11D**). Hence, the CHI-GA coating endows the MTX sensor with an adsorption-controlled behavior. Subsequently, the influence of the adsorption time on the electrochemical response was assessed on a

modified MN sensor. **Figure S12A** displays the SWV of 500 μM MTX at different adsorption times (i.e. 0 - 20 min). **Figure S12B** shows the I_p (left peak at 0.75 V) through time proving the adsorption of MTX. Ten minutes were selected for further experiments as a compromise between time and sensitivity. The oxidation peak at the lowest potential (I_p=0.75 V) was selected as the main analytical signal.

Overall, the use of a crosslinked CHI/GA coating on an electrode indeed produces a synergic effect for the detection of MTX: (i) the coating acts as an anti-biofouling layer, thus small molecules such as MTX diffuse toward the electrode's surface while blocking the entrance of macromolecules such as protein which is the main cause of biofouling;[40] (ii) it allows the adsorption of MTX at the surface of the electrode causing an increment in the sensitivity; and in turn (iii) the decrease in the oxidation potential.

***In vitro* analytical characterization of the MN sensing patch**.

To evidence the role of CHI/GA on the electrochemical performance of the sensor, we first evaluate the analytical features of the bare MN electrochemical sensor without the crosslinked CHI/GA coating (**Figure S13**). Although the linear range expanded from 25 μM to 300 μM which fits with the MTX levels during chemotherapy,[29,31,41] the bare MN sensor exhibited poor performance after piercing in porcine skin (**Figure S14**). Porcine skin has fatty components and proteins that might be adsorbed on the graphite paste of the working electrode, therefore, blocking the surface available for the oxidation of MTX. For this reason, the use of an anti-biofouling layer is necessary for the analysis of MTX in biofluids. Full *in vitro* analytical characterization of the bare MN sensor is described in the SI.

The deposition of the crosslinked CHI/GA layer proved to enhance the MTX detection in SPE. Therefore, the same coating was deposited on the MN sensors, and subsequently, the analytical performance was characterized (**Figure 2**). The CHI/GA allows the adsorption of MTX into the layer close to the electrode's surface and prevents macromolecules such as proteins, the main cause of biofouling, to be adsorbed at the surface (**Figure 2A**). **Figure 2B** illustrates the deposited coating on the MN sensor covering the entire surface of the WE. The analytical characterization of the f-MN sensor was first evaluated in PBS pH 7.4 at room temperature (i.e. 21 °C) by interrogating the MN sensor after 10 min adsorption time (**Figure 2C**). **Figure 2D** displays the calibration curve exhibiting a slope of 3.6 nA μM^{-1} within a dynamic range from 25 to 500 μM and a LOD of 10.0 μM which fits the therapeutic range of interest. As the f-MN sensor aims to be piercing the skin, the same f-MN sensor was assessed under 34 °C as the average skin temperature.[42] **Figure 2E** shows the SWV upon increasing concentrations of MTX with the representation of the I_p for the calibration curve in **Figure 2F**. At 34 °C, the slope substantially increased to 4.5 nA μM^{-1} while maintaining a similar dynamic range and LOD (12.1 μM). It has been reported that an increment in temperature provides higher mass transfer

7

in the Nernst layer[43] as well as it has been empirically shown its effect on the increment in peak current and the shift toward more negative potentials employing SWV.[44] Therefore, the f-MN sensor demonstrates analytical capabilities to be used at skin temperature. However, the following experiments were performed at room temperature for easy handling of the setup. The selectivity test was executed by adding 100 µM of the interferent (or 200 µM for glycine) to 100 µM MTX before the electrochemical interrogation. **Figure 2G** depicts the SWV and **Figure 2H** shows the I_p obtaining a RSD of 7.8% between all measurements. Thus, the f-MN sensor did not exhibit interferences on the MTX signal with regularly encountered electroactive molecules in biofluids. As one of the features of the CHI/GA is the anti-biofouling capacity, PBS with BSA as biofouling agent was employed for the testing. **Figure 2I** shows the SWVs of the f-MN sensor in the BSA in solution and the corresponding calibration curve is illustrated in **Figure 2J**. A slope of 2.3 nA µM^{-1} and LOD of 19.9 µM showed an effect of the protein on the analytical performance, although the CHI/GA still allowed for MTX detection in the therapeutic range. The repeatability of the f-MN sensor was assessed for 25, 100 and 300 µM in PBS-BSA (**Figure 2K** and zoom in **Figure 2L**). The results showed excellent repeatability (i.e. RSD$_{25µM}$ = 4.8%, RSD$_{100µM}$ = 5.5%, and RSD$_{300µM}$ = 4.3%).
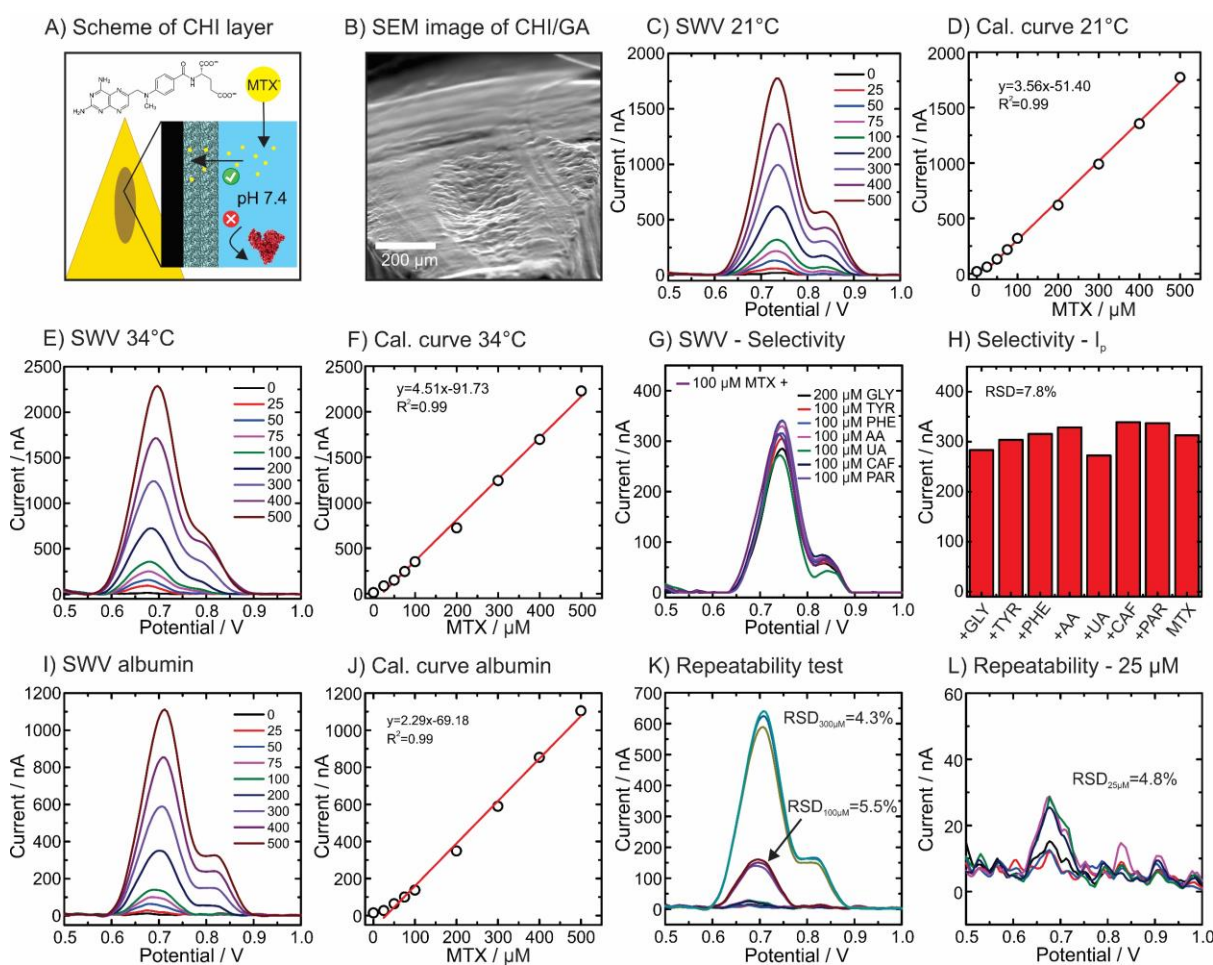
Figure 2. In vitro analytical characterization of the functionalized MN-based electrochemical sensor with the crosslinked CHI/GA coating in PBS pH 7.4. (A) Diagram of the anti-biofouling mechanism employing the crosslinked CHI/GA coating. (B) SEM image of the CHI/GA layer. (C) SWVs of increasing concentrations of MTX at 21 °C and (D) Corresponding calibration curve. (E) SWVs of increasing concentrations of MTX at 34 °C and (D) Corresponding calibration curve. (G) SWV from the selectivity test by using 100 μM MTX and interferent and (H) Corresponding peak current from the anodic event. All previous experiments were performed in PBS pH 7.4. Test under biofouling agent (20.6 g L^{-1} of BSA): (I) SWVs of increasing concentrations of MTX at 21 °C and (J) Corresponding calibration curve. Repeatability test (N = 3) with (K) 100 μM, 200 μM and (L) 25 μM MTX.

To emulate the ability of the f-MN sensor for continuous monitoring of MTX, the performance of the f-MN sensor was investigated in AISF. **Figure 3A** depicts the SWVs of the f-MN sensor upon increasing concentrations of MTX. **Figure 3B** shows the calibration curve with a slope of 2.4 nA μM^{-1}, LOD of 10.2 μM within a linear range from 25 to 200 μM. It is important to mention that different f-MN sensors were used for the tests in buffer and AISF, thus differences in the sensitivity of the systems can be obtained. As the manufacturing process is performed in-house, variations in the fabrication process can lead to different electrochemical performances. Subsequently, the f-MN sensor was tested in AISF with BSA (**Figure 3C**). The slope of 1.8 nA μM^{-1} and LOD of 12.3 μM showed a decrease in the analytical performance similar to the behavior studied using PBS and PBS-BSA solutions. Despite this performance, the f-MN sensor allowed the monitoring of MTX within the range of interest (**Figure 3D**).

An important feature of a transdermal device aiming for continuous monitoring is the ability to detect fluctuations in the target analyte. Hence, a reversibility test in AISF with BSA was attained during eight cycles of increasing and decreasing concentrations of MTX (50 μM – 100 μM – 200 μM cycle) (**Figure 3E**). Subsequently, a calibration curve was constructed by plotting the I_p gathered from the reversibility test. **Figure 3F** displays a slope of 1.8 nA μM^{-1} which is the same value as for the previous calibration curve before the reversibility test, proving the stability of the f-MN sensor. Moreover, excellent repeatability of each concentration was obtained (RSD$_{50μM}$ = 10.9%, N = 5; RSD$_{100μM}$ = 7.5%, N = 8; and RSD$_{300μM}$ = 3.5%, N = 4).

Long-term stability is essential for wearable devices that aim to continuously monitor targets once are inserted or applied to the body. Therefore, the evaluation of the performance of the f-MN sensor in the AISF enriched with BSA was further studied during long-term analysis. First, the stability of the electrochemical readout was assessed continuously every 10 min without any MTX for 16 h (**Figure 3G**). This experiment provided information on the potential degradation of the CHI/GA layer and the rise of background peaks that could lead to false positives. Importantly, **Figure S15A** displays the SWVs of the blank without the emergence of

any background peak. Thereafter, the f-MN sensor was analyzed under 50 µM MTX for 5 h, exhibiting a repeatable peak current with a RSD of 11.1% (**Figure 3H**). The f-MN sensor was subsequently analyzed under 100 µM MTX for 13 h, exhibiting a repeatable peak current with a RSD of 4.7% (**Figure 3I**). Finally, the f-MN sensor was interrogated with 200 µM MTX for 13 h, exhibiting a RSD of 4.0% on the peak current (**Figure 3H**). Moreover, the SWVs exhibited a constant oxidation potential of the MTX signal between 0.72 V and 0.74 V (**Figure S15B – S15D**). **Figure S15E** represents the data distribution of the I_p at each concentration. Finally, the average I_p obtained during the stability tests was used to construct a calibration plot (**Figure 3K**). The calibration curve exhibited a slope of 1.8 nA µM^{-1} which is the same slope as the previous experiments, proving the stability of the f-MN sensor after more than three days of operation (i.e. two days during the stability test and one day for the reversibility test). Overall, the f-MN sensor proved to be a highly stable sensor for the monitoring and detection of fluctuations of MTX in protein-enriched media.
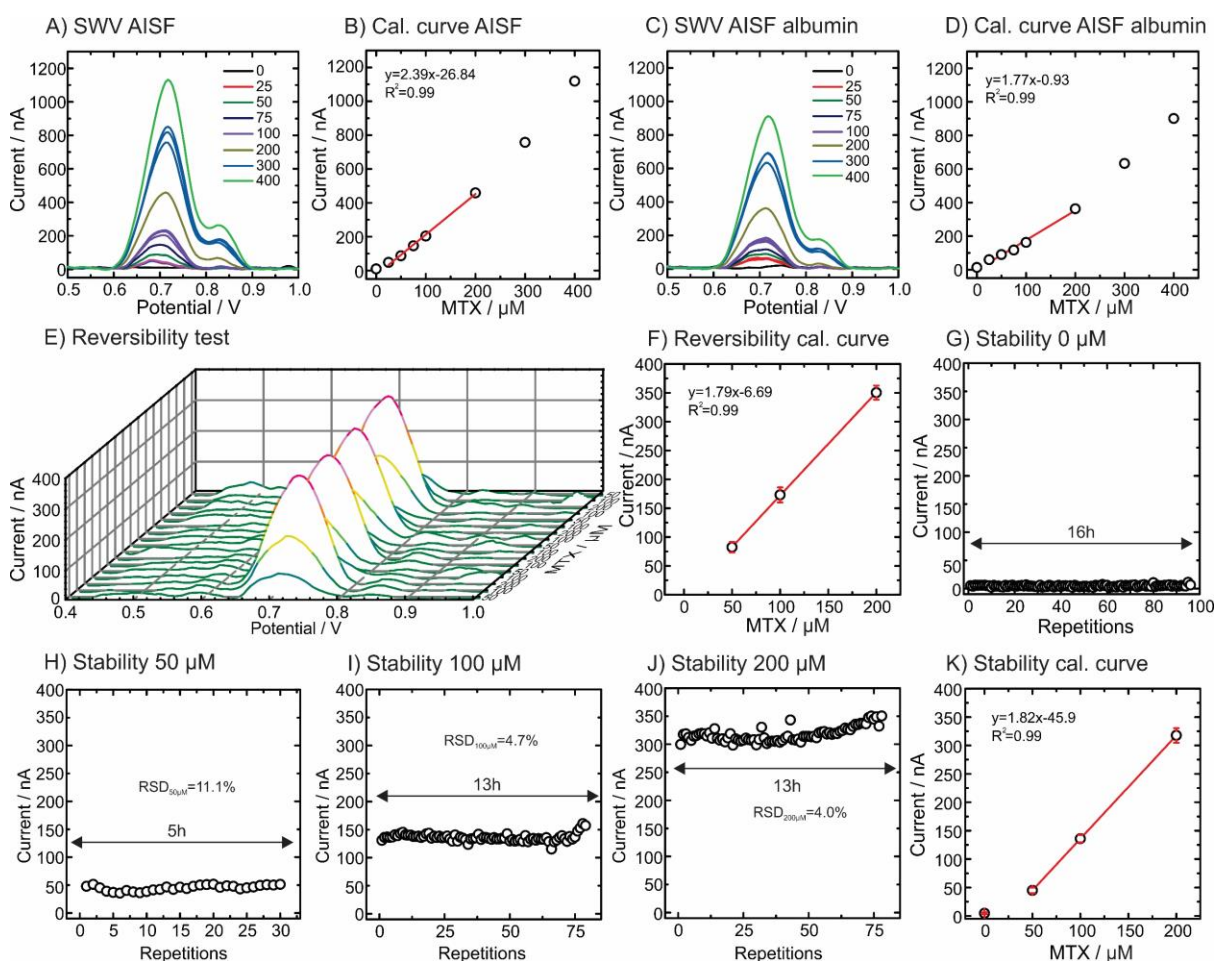
Figure 3. *Analytical performance of the f-MN sensor in artificial interstitial fluid (AISF): (A) SWVs and (B) Corresponding calibration curve in AISF. (C) SWV and (D) Corresponding calibration curves in AISF containing BSA (20.6 g L^{-1}). (E) Reversibility test from 50 to 200 µM (8 cycles) and (F) Corresponding calibration curve in AISF containing BSA. Stability test in AISF containing BSA for (G) 0 µM, (H) 50 µM, (I) 100 µM, (J) 200 µM and (K) Corresponding*

10

calibration curve using the I_p values from the stability tests. The interval time between electrochemical experiments was set to 10 min.

Ex vivo analytical characterization of the MN sensing patch.

The *ex vivo* test is an essential step in the characterization of MN-based devices. Franz diffusion cells are well-established setups used in *ex vivo* tests to emulate a real scenario while controlling the concentration of the analyte at the receptor compartment (**Figure S7**). Importantly, the setup mimics physiological conditions by employing porcine skin and a heating system. Traditionally, Franz diffusion cells have been employed in drug delivery studies.[45,46] However, this approach has also been recently used for the characterization of sensors.[47] In the latter case, the concentration at the receptor compartment can be varied by spiking the analyte through the sampling port to increase the concentration at the inner side of the skin or the concentration can be diluted by the extraction of the solution and introducing fresh solution (without the analyte) to the Franz cell. **Figure 4A** illustrates the Franz diffusion cell setup where the f-MN sensor is situated in the donor compartment (previously pierced into the porcine skin). Through the skin, the f-MN sensor can detect MTX that is present in the solution in the receptor compartment. **Figure S16A** depicts an image of the electrochemical setup in the Franz cell. **Figure S16B** shows a zoom on a Franz cell with the f-MN sensor inserted into the skin. Before adding the sensor to the Franz cell, the f-MN sensor is pierced into the skin previously attached to the donor compartment (**Figure S16C**), and subsequently deposited on the receptor compartment. Once the f-MN sensor was established on the Franz cell and connected to the potentiostat, a calibration curve was executed. **Figure 4B** displays the SWVs from the increasing concentrations of MTX in the receptor compartment. In real applications, the drug levels in a patient under MTX treatment expand from high concentration (mM range) due to the administration of a high-dose MTX to low µM levels due to the metabolization of the drug. These levels determine the toxicity of MTX to the body with an immediate rescue with leucovorin.[29,31] Therefore, the interest is to rapidly detect toxic levels of MTX by monitoring the clearance of MTX from the human body, meaning the monitoring of MTX levels in the ISF from high concentration to low concentration.[48] Hence, the f-MN sensor was interrogated with SWV under decreasing concentrations of MTX, ranging from 400 µM to 25 µM MTX in the Franz cell setup (**Figure 4C**). The calibration curves from the increasing and decreasing concentrations of MTX exhibited a slope of 1.75 nA µM⁻¹ and 1.76 nA µM⁻¹ with LODs of 22.5 µM and 9.3 µM, respectively, proving the analytical capability of the f-MN sensor to monitor the decrease of MTX levels in the receptor compartment through the skin. Finally, **Figure S16D** displays the status of the pierced skin after the *ex vivo* test, showing the holes from the MNs. Overall, the f-MN sensor was able to monitor increasing, and importantly,

decreasing concentrations of MTX through the skin which validates its potential use to monitor MTX clearance in patients.
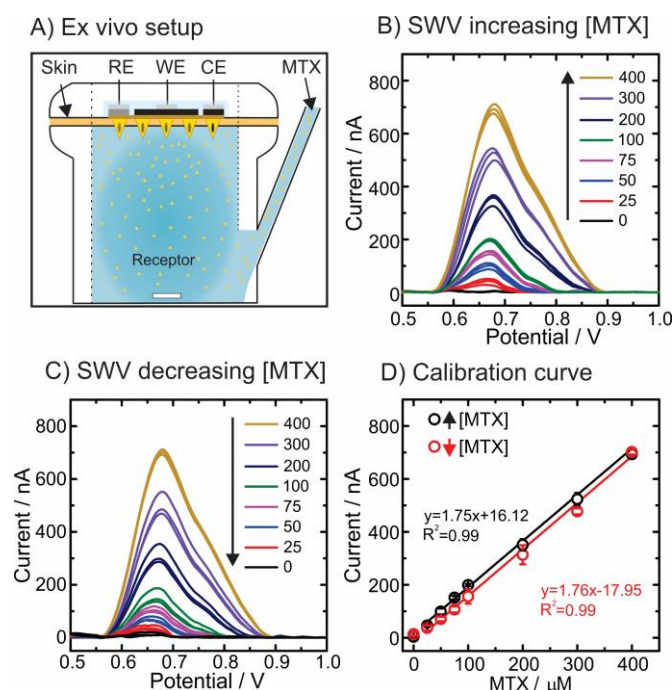
Figure 4. Ex vivo analytical characterization of the f-MN sensor in a Franz diffusion cell using porcine skin. (A) Schematics of the ex vivo setup. (B) SWVs of increasing concentrations of MTX in the cell. (C) SWVs of decreasing concentrations of MTX in the cell. (D) Corresponding calibration curves for increasing and decreasing MTX concentration. The interval time between electrochemical experiments was set to 10 min.

Transdermal on-demand drug delivery of methotrexate

The transdermal drug delivery was attained by using an IHMAS previously developed by the authors for model drugs such as methylene blue, fluorescein sodium, lidocaine hydrochloride, and BSA-FITC.[46] Following a similar IHMAS, the delivery of negatively charged MTX was tested by loading the reservoir of the patch with a MTX-containing hydrogel (**Figure S6**).

The concept was first tested in an *in vitro* setup using agarose gel. The IHMAS in the cathodic configuration (use of AgCl electrode) was pierced into the agarose gel and subsequently, 1 mA cm^{-2} was applied for an hour.[46] The negatively charged MTX is loaded on a hydrogel and in contact with the cathode. When the current is applied to the system, the electric field and the reduction of the AgCl to Ag releases Cl^{-}, which promotes the migration of MTX^{-} outwards to the solution in the receptor compartment. **Figure S17** shows the 5-fold enhanced delivery of MTX when the iontophoretic current was applied (i.e. the control delivered 66.6 ± 8.1 μg mL^{-1} *versus* the IHMAS delivered 317.2 ± 31.6 μg mL^{-1}), proving the working principle on MTX. In comparison to other drugs, MTX was passively delivered at a much higher amount which is

potentially related to the high loading of MTX in the hydrogel (5% in comparison to 0.5% in our previous work). In addition, MTX was highly delivered during the iontophoretic current due to the migration effect.

Porcine skin was used for the *ex vivo* test to emulate transdermal drug delivery. **Figure 5A** illustrates the experimental setup of the IHMAS on a Franz diffusion cell to prove the tailored delivery upon the application of current. **Figure S18A** shows an image of the Franz cell setup with IHMAS (cathode) piercing the skin. In this case, the entire IHMAS works as the cathode (AgCl electrode) for the iontophoresis. The anode consisted of a Ag wire introduced through the sampling port to the solution. The evaluation of the iontophoretic effect was tested on the IHMAS by passive delivery as the control (no current) and active delivery (1 mA cm^{-2}). **Figure 5B** displays the drug delivery profiles, exhibiting a dramatic enhancement over a 6 h period when current is applied. The IHMAS presented a constant and linear delivery of MTX during the 6 h with a 26-fold significant increment in the permeation of MTX at 6 h in comparison to the control (118.6 ± 24.2 µg mL^{-1} *versus* 4.5 ± 1.4 µg mL^{-1}, N = 5, *p*-value < 0.05). **Figure S18B** depicts the skin after the 6 h tests and the MTX-loaded hydrogel. The skin employed during the iontophoresis condition exhibited stronger yellowish color than the control, although the yellowish color was also present in the control (**Figure S18C**). This is due to the passive diffusion of the highly concentrated MTX from the hydrogel. Nevertheless, the power of the iontophoresis was clearly enhancing the delivery through the skin (less permeable and less hydrophilic than agarose gel) in comparison to the *in vitro* test (i.e. 26-fold *versus* 5-fold enhancement) as it is shown in **Figure 5B**. Therefore, the iontophoretic effect drastically increases the transdermal delivery of charged MTX through the skin.

The IHMAS concept was subsequently translated into a fully integrated two-electrode system (anode and cathode in the same HMA patch). In this new design, a septum separated the anode compartment from the cathode compartment, and the cap incorporated the Ag electrode (anode) and the AgCl electrode (cathode). This design enables iontophoresis in a fully miniaturized system. **Figure 5C** illustrates the MN device pierced into the skin of a Franz cell. In this case, the MTX-loaded hydrogel is situated in the cathode compartment, and a blank hydrogel is in the anode compartment to ensure the electrochemical connection between the electrodes. The dimensions of the design of the one-electrode and two-electrode IHMAS are described in **Figure S6**. The drug delivery profiles during the *ex vivo* test exhibited an increment of the MTX permeation when applying 1 mA cm^{-2} through the system (**Figure 5D**). At 4 h, the IHMAS delivered significantly 3.8-fold higher amount than the control (i.e. 67.7 ± 22.7 µg mL^{-1} *versus* 17.9 ± 5.0 µg mL^{-1}, N = 5, *p*-value < 0.05). The incorporation of the two-electrode IHMAS increased the error in the delivery of MTX. It is suggested that fewer hollow MNs are employed to pierce the skin in the two-electrode configuration (i.e. from 25 MNs in a single patch to 10 MNs), thus the error in the delivery might be increased if a few MNs are not

properly inserted into the skin. This effect needs to be considered for future designs of drug delivery patches.
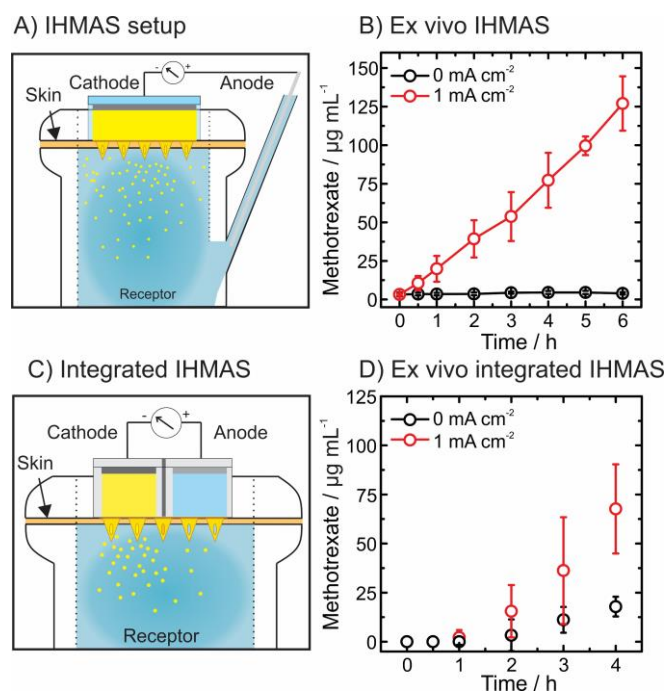
Figure 5. *Ex vivo permeation test using the iontophoretic hollow microneedle array system (IHMAS). (A) Schematics of the ex vivo setup for the IHMAS as the cathode on a Franz diffusion cell. (B) Enhanced permeation of methotrexate while applying 1 mA cm^{-2} of iontophoretic current on the IHMAS (N = 5). Proof of concept of the two-electrode integrated IHMAS. (C) Schematics of the ex vivo test for the integrated IHMAS on a Franz diffusion cell. The drug-loaded hydrogel is situated in the cathode compartment and a blank hydrogel is in the anode compartment. (D) Skin permeation of methotrexate employing the integrated IHMAS over 4 h in a Franz cell setup (N = 3).*

CONCLUSIONS

We have demonstrated, for the first time, the development of MN-based electrochemical sensors for the transdermal monitoring and delivery of MTX. The functionalization of the MN sensor with a CHI/GA coating conferred a synergic effect of anti-biofouling and adsorption capabilities for the continuous operation of the f-MN sensor. First, a HMA was modified with conductive pastes to create a three-electrode electrochemical system in a single patch. Thereafter, the MN sensor was analytically characterized with and without the CHI/GA to unravel its unique properties for the detection of MTX in protein-enriched AISF. This is a critical step for the evaluation of the f-MN sensor in real ISF. The full *in vitro* analysis exhibited remarkable results within the linear range of high-dose MTX administration levels in cancer patients. The reversibility and long-term stability of the readout exhibited an outstanding performance which is essential for wearable devices. The f-MN sensor was assessed under

an *ex vivo* configuration in porcine skin, proving the ability to transdermally monitor decreasing concentrations of MTX, an essential feature to track MTX clearance in patients. Finally, the development of an on-demand iontophoretic system based on the same HMA patch shows the versatility of the MN technology. Significantly, the IHMAS and f-MN sensors show the first steps toward a closed-loop sensing and delivery system for the self-sufficient management of MTX therapy in cancer patients. The next steps involve the decrease of the LOD to expand the closed-loop system to other disorders such as rheumatoid arthritis where autonomous therapeutic drug monitoring can facilitate the lifestyle of these patients. The incorporation of algorithms with closed-loop systems that can allow the monitoring of the therapeutic drug and the on-demand administration when the levels of the drug are low would provide a deep impact on how therapies are handled. Overall, the MN technology presented here demonstrates the value of MN patches to enhance personalized medicine and depicts the potential to revolutionize healthcare from localized episodic to decentralized continuous treatments.

ASSOCIATED CONTENT

Supporting Information. This material is available free of charge via the Internet at http://pubs.acs.org.

°Details of the experimental section, optical and electrochemical characterization of the sensor and the MN sensing patch, and images of the *ex vivo* test.

AUTHOR INFORMATION

Corresponding Author

*Marc Parrilla − A-Sense Lab, Department of Bioscience Engineering, University of Antwerp, 2020 Antwerp, Belgium. Email: marc.parrillapons@uantwerpen.be

*Karolien De Wael − A-Sense Lab, Department of Bioscience Engineering, University of Antwerp, 2020 Antwerp, Belgium. Email: karolien.dewael@uantwerpen.be

*Ryan F. Donnelly − School of Pharmacy, Medical Biology Centre, Queen's University Belfast, Belfast BT9 7BL, United Kingdom. Email: r.donnelly@qub.ac.uk

Author Contributions

M.P. designing methodology and concept, development of the sensor, analytical characterization of the sensor, and writing the manuscript. U.D. and J.D-R. designing the HMN array, designing experiments, characterization of the HMN arrays, and revision of the manuscript. S.T. optical characterization of the sensor. R.F.D. and K.D.W. revision of the manuscript and supervision. The manuscript was written through the contributions of all authors. All authors have approved the final version of the manuscript.

ABBREVIATIONS

Artificial interstitial fluid, AISF; attenuated total reflectance - Fourier transform infrared spectroscopy, ATR-FTIR; bovine serum albumin, BSA; chitosan, CHI; cyclic voltammetry, CV; counter electrode, CE; functionalized microneedle, f-MN; Glutaraldehyde, GA; hollow microneedle arrays, HMA; iontophoretic hollow microneedle array system, IHMAS; interstitial fluid, ISF; limit of detection, LOD; microneedle, MN; methotrexate, MTX; polyether ether ketone, PEEK; reference electrode, RE; scanning electron microscopy, SEM; square-wave voltammetry, SWV; working electrode, WE.

REFERENCES

(1)   Sempionatto, J. R.; Lasalde-Ramírez, J. A.; Mahato, K.; Wang, J.; Gao, W. Wearable Chemical Sensors for Biomarker Discovery in the Omics Era. *Nat. Rev. Chem.* **2022**, *6* (12), 899–915. https://doi.org/10.1038/s41570-022-00439-w.

(2)   Parrilla, M.; De Wael, K. Wearable Self-Powered Electrochemical Devices for Continuous Health Management. *Adv. Funct. Mater.* **2021**, *31* (50), 2107042. https://doi.org/10.1002/adfm.202107042.

(3)   Hoss, U.; Budiman, E. S. Factory-Calibrated Continuous Glucose Sensors: The Science Behind the Technology. *Diabetes Technol. Ther.* **2017**, *19* (S2), S-44-S-50. https://doi.org/10.1089/dia.2017.0025.

(4)   Liao, Z.; Zhou, Q.; Gao, B. Electrochemical Microneedles: Innovative Instruments in Health Care. *Biosensors* **2022**, *12* (10), 801. https://doi.org/10.3390/bios12100801.

(5)   Abdullah, H.; Phairatana, T.; Jeerapan, I. Tackling the Challenges of Developing Microneedle-Based Electrochemical Sensors. *Microchim. Acta* **2022**, *189* (11), 440. https://doi.org/10.1007/s00604-022-05510-3.

(6)   Wang, J.; Lu, Z.; Cai, R.; Zheng, H.; Yu, J.; Zhang, Y.; Gu, Z. Microneedle-Based Transdermal Detection and Sensing Devices. *Lab Chip* **2023**, *23* (5), 869–887.

https://doi.org/10.1039/D2LC00790H.

(7)   Zou, Y.; Chu, Z.; Guo, J.; Liu, S.; Ma, X.; Guo, J. Minimally Invasive Electrochemical Continuous Glucose Monitoring Sensors: Recent Progress and Perspective. *Biosens. Bioelectron.* **2023**, *225* (January), 115103. https://doi.org/10.1016/j.bios.2023.115103.

(8)   Tehrani, F.; Teymourian, H.; Wuerstle, B.; Kavner, J.; Patel, R.; Furmidge, A.; Aghavali, R.; Hosseini-Toudeshki, H.; Brown, C.; Zhang, F.; et al. An Integrated Wearable Microneedle Array for the Continuous Monitoring of Multiple Biomarkers in Interstitial Fluid. *Nat. Biomed. Eng.* **2022**, *6* (11), 1214–1224. https://doi.org/10.1038/s41551-022-00887-1.

(9)   Lin, S.; Cheng, X.; Zhu, J.; Wang, B.; Jelinek, D.; Zhao, Y.; Wu, T.-Y.; Horrillo, A.; Tan, J.; Yeung, J.; et al. Wearable Microneedle-Based Electrochemical Aptamer Biosensing for Precision Dosing of Drugs with Narrow Therapeutic Windows. *Sci. Adv.* **2022**, *8* (38), eabq4539. https://doi.org/10.1126/sciadv.abq4539.

(10)   Parrilla, M.; Vanhooydonck, A.; Johns, M.; Watts, R.; Wael, K. De. 3D-Printed Microneedle-Based Potentiometric Sensor for PH Monitoring in Skin Interstitial Fluid. *Sensors Actuators B. Chem.* **2023**, *378*, 133159. https://doi.org/10.1016/j.snb.2022.133159.

(11)   Goud, K. Y.; Mahato, K.; Teymourian, H.; Longardner, K.; Litvan, I.; Wang, J. Wearable Electrochemical Microneedle Sensing Platform for Real-Time Continuous Interstitial Fluid Monitoring of Apomorphine: Toward Parkinson Management. *Sensors Actuators B Chem.* **2022**, *354*, 131234. https://doi.org/10.1016/j.snb.2021.131234.

(12)   Parrilla, M.; Detamornrat, U.; Domínguez-Robles, J.; Donnelly, R. F.; De Wael, K. Wearable Hollow Microneedle Sensing Patches for the Transdermal Electrochemical Monitoring of Glucose. *Talanta* **2022**, *249*, 123695. https://doi.org/10.1016/j.talanta.2022.123695.

(13)   Zheng, L.; Zhu, D.; Wang, W.; Liu, J.; Thng, S. T. G.; Chen, P. A Silk-Microneedle Patch to Detect Glucose in the Interstitial Fluid of Skin or Plant Tissue. *Sensors Actuators B Chem.* **2022**, *372* (June), 132626. https://doi.org/10.1016/j.snb.2022.132626.

(14)   Friedel, M.; Thompson, I. A. P.; Kasting, G.; Polsky, R.; Cunningham, D.; Soh, H. T.; Heikenfeld, J. Opportunities and Challenges in the Diagnostic Utility of Dermal Interstitial Fluid. *Nat. Biomed. Eng.* **2023**. https://doi.org/10.1038/s41551-022-00998-9.

(15)   Teymourian, H.; Parrilla, M.; Sempionatto, J. R.; Montiel, N. F.; Barfidokht, A.; Van Echelpoel, R.; De Wael, K.; Wang, J. Wearable Electrochemical Sensors for the Monitoring and Screening of Drugs. *ACS Sensors* **2020**, *5*, 2679−2700. https://doi.org/10.1021/acssensors.0c01318.

(16) Joosten, F.; Parrilla, M.; Nuijs, A. L. N. Van; Ozoemena, K. I.; Wael, K. De. Electrochemical Detection of Illicit Drugs in Oral Fluid : Potential for Forensic Drug Testing. *Electrochim. Acta* **2022**, *436* (September), 141309. https://doi.org/10.1016/j.electacta.2022.141309.

(17) Ma, S.; Li, J.; Pei, L.; Feng, N.; Zhang, Y. Microneedle-Based Interstitial Fluid Extraction for Drug Analysis: Advances, Challenges, and Prospects. *J. Pharm. Anal.* **2023**, *13* (2), 111–126. https://doi.org/10.1016/j.jpha.2022.12.004.

(18) Goud, K. Y.; Moonla, C.; Mishra, R. K.; Yu, C.; Narayan, R.; Litvan, I.; Wang, J. Wearable Electrochemical Microneedle Sensor for Continuous Monitoring of Levodopa: Toward Parkinson Management. *ACS Sensors* **2019**, *4* (8), 2196–2204. https://doi.org/10.1021/acssensors.9b01127.

(19) Wu, Y.; Tehrani, F.; Teymourian, H.; Mack, J.; Shaver, A.; Reynoso, M.; Kavner, J.; Huang, N.; Furmidge, A.; Duvvuri, A.; et al. Microneedle Aptamer-Based Sensors for Continuous, Real-Time Therapeutic Drug Monitoring. *Anal. Chem.* **2022**, *94* (23), 8335–8345. https://doi.org/10.1021/acs.analchem.2c00829.

(20) Park, S. H.; Kim, Y. J.; Kostal, E.; Matylitskaya, V.; Partel, S.; Ryu, W. H. Highly-Sensitive Single-Step Sensing of Levodopa by Swellable Microneedle-Mounted Nanogap Sensors. *Biosens. Bioelectron.* **2023**, *220*, 114912. https://doi.org/10.1016/j.bios.2022.114912.

(21) Gowda, B. H. J.; Ahmed, M. G.; Sahebkar, A.; Riadi, Y.; Shukla, R.; Kesharwani, P. Stimuli-Responsive Microneedles as a Transdermal Drug Delivery System: A Demand-Supply Strategy. *Biomacromolecules* **2022**, *23* (4), 1519–1544. https://doi.org/10.1021/acs.biomac.1c01691.

(22) Yang, J.; Zhang, H.; Hu, T.; Xu, C.; Jiang, L.; Shrike Zhang, Y.; Xie, M. Recent Advances of Microneedles Used towards Stimuli-Responsive Drug Delivery, Disease Theranostics, and Bioinspired Applications. *Chem. Eng. J.* **2021**, *426* (June), 130561. https://doi.org/10.1016/j.cej.2021.130561.

(23) Yang, J.; Yang, J.; Gong, X.; Zheng, Y.; Yi, S.; Cheng, Y.; Li, Y.; Liu, B.; Xie, X.; Yi, C.; et al. Recent Progress in Microneedles-Mediated Diagnosis, Therapy, and Theranostic Systems. *Adv. Healthc. Mater.* **2022**, *11* (10), 2102547. https://doi.org/10.1002/adhm.202102547.

(24) Li, X.; Huang, X.; Mo, J.; Wang, H.; Huang, Q.; Yang, C.; Zhang, T.; Chen, H. J.; Hang, T.; Liu, F.; et al. A Fully Integrated Closed-Loop System Based on Mesoporous Microneedles-Iontophoresis for Diabetes Treatment. *Adv. Sci.* **2021**, *8* (16), 2100827. https://doi.org/10.1002/advs.202100827.

(25) Luo, X.; Yu, Q.; Liu, Y.; Gai, W.; Ye, L.; Yang, L.; Cui, Y. Closed-Loop Diabetes Minipatch Based on a Biosensor and an Electroosmotic Pump on Hollow

Biodegradable Microneedles. *ACS Sensors* **2022**, *7* (5), 1347–1360. https://doi.org/10.1021/acssensors.1c02337.

(26) Luo, X.; Yu, Q.; Yang, L.; Cui, Y. Wearable, Sensing-Controlled, Ultrasound-Based Microneedle Smart System for Diabetes Management. *ACS Sensors* **2023**. https://doi.org/10.1021/acssensors.2c02863.

(27) Teymourian, H.; Tehrani, F.; Longardner, K.; Mahato, K.; Podhajny, T.; Moon, J. M.; Kotagiri, Y. G.; Sempionatto, J. R.; Litvan, I.; Wang, J. Closing the Loop for Patients with Parkinson Disease: Where Are We? *Nat. Rev. Neurol.* **2022**, *18* (8), 497–507. https://doi.org/10.1038/s41582-022-00674-1.

(28) Hamed, K. M.; Dighriri, I. M.; Baomar, A. F.; Alharthy, B. T.; Alenazi, F. E.; Alali, G. H.; Alenazy, R. H.; Alhumaidi, N. T.; Alhulayfi, D. H.; Alotaibi, Y. B.; et al. Overview of Methotrexate Toxicity: A Comprehensive Literature Review. *Cureus* **2022**, *14* (9), e29518. https://doi.org/10.7759/cureus.29518.

(29) LaCasce, A. S. Therapeutic Use and Toxicity of High-Dose Methotrexate. *UpToDate* **2022**, Accessed 08-04-2023.

(30) Du, H.; Liu, P.; Zhu, J.; Lan, J.; Li, Y.; Zhang, L.; Zhu, J.; Tao, J. Hyaluronic Acid-Based Dissolving Microneedle Patch Loaded with Methotrexate for Improved Treatment of Psoriasis. *ACS Appl. Mater. Interfaces* **2019**, *11* (46), 43588–43598. https://doi.org/10.1021/acsami.9b15668.

(31) Treon, S. P.; Chabner, B. A. Concepts in Use of High-Dose Methotrexate Therapy. *Clin. Chem.* **1996**, *42* (8 SPEC. ISS.), 1322–1329. https://doi.org/10.1093/clinchem/42.8.1322.

(32) Chamorro-Garcia, A.; Gerson, J.; Flatebo, C.; Fetter, L.; Downs, A. M.; Emmons, N.; Ennis, H. L.; Milosavić, N.; Yang, K.; Stojanovic, M.; et al. Real-Time, Seconds-Resolved Measurements of Plasma Methotrexate in Situ in the Living Body. *ACS Sensors* **2023**, *8* (1), 150–157. https://doi.org/10.1021/acssensors.2c01894.

(33) Khand, A. A.; Lakho, S. A.; Tahira, A.; Ubaidullah, M.; Alothman, A. A.; Aljadoa, K.; Nafady, A.; Ibupoto, Z. H. Facile Electrochemical Determination of Methotrexate (MTX) Using Glassy Carbon Electrode-Modified with Electronically Disordered NiO Nanostructures. *Nanomaterials* **2021**, *11* (5), 1266. https://doi.org/10.3390/nano11051266.

(34) Deng, Z.; Li, H.; Tian, Q.; Zhou, Y.; Yang, X.; Yu, Y.; Jiang, B.; Xu, Y.; Zhou, T. Electrochemical Detection of Methotrexate in Serum Sample Based on the Modified Acetylene Black Sensor. *Microchem. J.* **2020**, *157* (1677), 105058. https://doi.org/10.1016/j.microc.2020.105058.

(35) Parrilla, M.; Vanhooydonck, A.; Watts, R.; De Wael, K. Wearable Wristband-Based Electrochemical Sensor for the Detection of Phenylalanine in Biofluids. *Biosens.*

Bioelectron. **2022**, *197*, 113764. https://doi.org/10.1016/j.bios.2021.113764.

(36) Felipe Montiel, N.; Parrilla, M.; Beltrán, V.; Nuyts, G.; Van Durme, F.; De Wael, K. The Opportunity of 6-Monoacetylmorphine to Selectively Detect Heroin at Preanodized Screen Printed Electrodes. *Talanta* **2021**, *226*, 122005. https://doi.org/10.1016/j.talanta.2020.122005.

(37) Hoffmann, B.; Seitz, D.; Mencke, A.; Kokott, A.; Ziegler, G. Glutaraldehyde and Oxidised Dextran as Crosslinker Reagents for Chitosan-Based Scaffolds for Cartilage Tissue Engineering. *J. Mater. Sci. Mater. Med.* **2009**, *20* (7), 1495–1503. https://doi.org/10.1007/s10856-009-3707-3.

(38) Islam, N.; Wang, H.; Maqbool, F.; Ferro, V. In Vitro Enzymatic Digestibility of Glutaraldehyde-Crosslinked Chitosan Nanoparticles in Lysozyme Solution and Their Applicability in Pulmonary Drug Delivery. *Molecules* **2019**, *24* (7), 1–17. https://doi.org/10.3390/molecules24071271.

(39) Jandaghi, N.; Jahani, S.; Foroughi, M. M.; Kazemipour, M.; Ansari, M. Cerium-Doped Flower-Shaped ZnO Nano-Crystallites as a Sensing Component for Simultaneous Electrochemical Determination of Epirubicin and Methotrexate. *Microchim. Acta* **2020**, *187* (1), 24. https://doi.org/10.1007/s00604-019-4016-2.

(40) Russo, M. J.; Han, M.; Desroches, P. E.; Manasa, C. S.; Dennaoui, J.; Quigley, A. F.; Kapsa, R. M. I.; Moulton, S. E.; Guijt, R. M.; Greene, G. W.; et al. Antifouling Strategies for Electrochemical Biosensing: Mechanisms and Performance toward Point of Care Based Diagnostic Applications. *ACS Sensors* **2021**, *6* (4), 1482–1507. https://doi.org/10.1021/acssensors.1c00390.

(41) Comandone, A.; Passera, R.; Boglione, A.; Tagini, V.; Ferrari, S.; Cattel, L. High Dose Methotrexate in Adult Patients with Osteosarcoma: Clinical and Pharmacokinetic Results. *Acta Oncol. (Madr).* **2005**, *44* (4), 406–411. https://doi.org/10.1080/02841860510029770.

(42) Bierman, W. The Temperature of the Skin Surface. *JAMA - J. Am. Med. Assoc.* **1936**, *106* (14), 1158–1162. https://doi.org/10.1001/jama.1936.02770140020007.

(43) Krejci, J.; Sajdlova, Z.; Krejci, J.; Marvanek, T. Voltammetry under a Controlled Temperature Gradient. *Sensors* **2010**, *10* (7), 6821–6835. https://doi.org/10.3390/s100706821.

(44) Schram, J.; Parrilla, M.; Slosse, A.; Van Durme, F.; Åberg, J.; Björk, K.; Bijvoets, S. M.; Sap, S.; Heerschop, M. W. J.; De Wael, K. Paraformaldehyde-Coated Electrochemical Sensor for Improved On-Site Detection of Amphetamine in Street Samples. *Microchem. J.* **2022**, *179*, 107518. https://doi.org/10.1016/j.microc.2022.107518.

(45) Tekko, I. A.; Chen, G.; Domínguez-Robles, J.; Raj Singh Thakur, R.; Hamdan, I. M.

N.; Vora, L.; Larrañeta, E.; McElnay, J. C.; McCarthy, H. O.; Rooney, M.; et al. Development and Characterisation of Novel Poly (Vinyl Alcohol)/Poly (Vinyl Pyrrolidone)-Based Hydrogel-Forming Microneedle Arrays for Enhanced and Sustained Transdermal Delivery of Methotrexate. *Int. J. Pharm.* **2020**, *586* (May), 119580. https://doi.org/10.1016/j.ijpharm.2020.119580.

(46)   Detamornrat, U.; Parrilla, M.; Domínguez-Robles, J.; Anjani, Q. K.; Larrañeta, E.; De Wael, K.; Donnelly, R. F. Transdermal On-Demand Drug Delivery Based on an Iontophoretic Hollow Microneedle Array System. *Lab Chip* **2023**, *23*, 2304–2315. https://doi.org/10.1039/D3LC00160A.

(47)   Hoang, V. C.; Shafaat, A.; Jankovskaja, S.; Gomes, V. G.; Ruzgas, T. Franz Cells for Facile Biosensor Evaluation: A Case of HRP/SWCNT-Based Hydrogen Peroxide Detection via Amperometric and Wireless Modes. *Biosens. Bioelectron.* **2021**, *191* (December 2020), 113420. https://doi.org/10.1016/j.bios.2021.113420.

(48)   Kolluru, C.; Williams, M.; Yeh, J. S.; Noel, R. K.; Knaack, J.; Prausnitz, M. R. Monitoring Drug Pharmacokinetics and Immunologic Biomarkers in Dermal Interstitial Fluid Using a Microneedle Patch. *Biomed. Microdevices* **2019**, *21* (1), 14. https://doi.org/10.1007/s10544-019-0363-3.

Table of Contents